Zhou, Jingyi; Liu, Kaijun; Jarvinen, Riku; Kallio, Esa; Cheng, Kun; Zhang, Shuai; Liu, Qi; Liu, Yuqi; Wang, Yan; Wang, Ruohan; Wang, Xinye; Shang, Xuanyu; Xu, Zhongyuan; Yuan, Yi

Hybrid Simulations of the Martian Magnetotail Twist

Published in:
Astrophysical Journal

DOI:
10.3847/1538-4357/ad8159

Published: 01/11/2024

Document Version
Publisher's PDF, also known as Version of record

The Astrophysical Journal, 976:7 (7pp), 2024 November 20 https://doi.org/10.3847/1538-4357/ad8159

Hybrid Simulations of the Martian Magnetotail Twist

Jingyi Zhou[1], Kaijun Liu[1], Riku Jarvinen[2], Esa Kallio[3], Kun Cheng[1], Shuai Zhang[1], Qi Liu[1], Yuqi Liu[1], Yan Wang[1], Ruohan Wang[1], Xinye Wang[1], Xuanyu Shang[1], Zhongyuan Xu[1], and Yi Yuan[4]
[1] Department of Earth and Space Sciences, Southern University of Science and Technology, Shenzhen, People's Republic of China; liukj@sustech.edu.cn
[2] Finnish Meteorological Institute, Helsinki, Finland
[3] Department of Electronics and Nanoengineering, School of Electrical Engineering, Aalto University, Espoo, Finland
[4] School of Atmospheric Sciences, Sun Yat-sen University, Zhuhai, People's Republic of China
Received 2024 May 31; revised 2024 September 09; accepted 2024 September 24; published 2024 November 11

Abstract

Three-dimensional global hybrid simulations are performed to explore how the interplanetary magnetic field (IMF), the Martian crustal fields, and planetary pickup ions affect the twisting of the Martian magnetotail. The results agree with previous studies that the crustal magnetic fields cause the Martian magnetotail to twist counterclockwise or clockwise depending on the sign of the IMF Y-component in the Mars solar orbital coordinates. However, the twist is more pronounced when the crustal fields are on the nightside, contradicting the early explanation that the crustal fields affect the twist through dayside magnetic reconnection between the crustal fields and the draped IMF. Additionally, planetary pickup ions also contribute to the twist because their mass loading slows down the plasma flow and leads to the bending of the magnetic field lines in the magnetotail. It is demonstrated that the twist inside Mars' shadow in the near magnetotail region (at $X = -1.5\,R_M$, where R_M is Mars' radius) is mainly attributable to the crustal fields, while the influence of planetary pickup ions starts to dominate outside Mars' shadow and in regions further away from Mars.

Unified Astronomy Thesaurus concepts: Planetary magnetospheres (997); Solar-planetary interactions (1472); Pickup ions (1239); Magnetic anomalies (993); Mars (1007)

1. Introduction

Unlike the Earth, which possesses a global intrinsic dipole magnetic field, Mars's inner dynamo to generate the global magnetic field ceased about 4.1 Gyr ago (R. J. Lillis et al. 2008). The lack of a global intrinsic magnetic field allows the solar wind (SW) plasma (and the interplanetary magnetic field (IMF) it carries) to interact with the Martian atmosphere and ionosphere directly, resulting in an induced Martian magnetosphere. The magnetotail of the Martian magnetosphere is formed by the draped IMF and is composed of two opposing lobes separated by a polarity reversal layer referred to as the neutral (current) sheet (N. Romanelli et al. 2015). On the other hand, Mars has relatively strong local crustal remnant magnetic fields (crustal magnetic anomalies) that rotate with the planet (M. H. Acuña et al. 1999). The local crustal magnetic fields make the Martian magnetosphere a hybrid magnetosphere with features of both induced and intrinsic origins (E. Dubinin et al. 2022) and lead to various changes in comparison with a purely induced magnetosphere (C. Dong et al. 2015; Y. Harada et al. 2015; T. Hara et al. 2017; P. Garnier et al. 2022; M. Wang et al. 2022; C. Zhang et al. 2022).

Recently, G. A. DiBraccio et al. (2018, 2022) reported a twisted magnetic field structure of the Martian magnetotail based on the Mars Atmosphere and Volatile Evolution (MAVEN) observations and suggested that dayside magnetic reconnection between the crustal fields and the draped IMF is responsible for the twist. The twist refers to a morphological change or a rotation of the magnetotail in the plane perpendicular to the upstream SW velocity (the tail cross section) from a purely IMF-driven orientation of an ideal, hemispherically symmetric induced magnetotail. The results of magnetohydrodynamic (MHD) simulations in S. Xu et al. (2020) provided a detailed map of the topology of the Martian magnetotail dominated by draped and open magnetic field lines, consistent with the explanation of G. A. Dibraccio et al. (2018, 2022) and supporting the picture of a "hybrid" magnetotail that is partly induced/draped and partly intrinsic/planetary in origin. Magnetotail twisting was also found at Earth and Mercury. However, due to the significant influence of their intrinsic magnetic fields on the structure of their magnetosphere over a large tail range, the twisting is relatively weak (E. Kallio et al. 2008; T. Pitkänen et al. 2021; N. Romanelli et al. 2022). Interestingly, E. Dubinin et al. (2022) showed that the distribution of the Martian magnetotail lobes generated by the lower-order crustal magnetic field model resembles the Earth's, while the purely induced magnetotail does not exhibit any twisted structure, emphasizing the indispensable role of the crustal fields in producing the Martian magnetotail twist.

Observations and simulations have revealed the existence of magnetotail twisting at Venus as well (e.g., S. D. Xiao et al. 2016; L. Chai et al. 2019). Since Venus has neither a global intrinsic magnetic field nor significant local crustal fields, this implies that some factors other than crustal fields, such as the upstream flow-aligned component of the IMF, can also cause magnetotail twisting (R. Jarvinen et al. 2013). Moreover, R. Ramstad et al. (2020) suggested that magnetotail twisting observed at Mars (and Venus) can be attributed to the sunward currents arising from the electrical coupling between the planetary ionosphere and the SW within an induced magnetosphere. Thus, a twisted tail structure may be a common characteristic of induced magnetospheres, rather than being unique to Mars due to its crustal fields. More recently,

A. R. Azari et al. (2023) identified an altitude-dependent draping morphology in the dayside Martian magnetosphere using MAVEN magnetic field data. They further argued that the observed dayside magnetic field distortions at high (>800 km) and low (<800 km) altitudes, which trace down the tail to cause the outer and inner magnetotail twists, are an induced response to the IMF direction and directly related to the crustal fields, respectively. In addition, planetary ions flowing out from the ionosphere and produced in the neutral exosphere (generally referred to as planetary pickup ions in the present study) have been suggested to modify the Martian and Venusian magnetospheres (e.g., S. H. Brecht 1990; E. Kallio & P. Janhunen 2002; E. Dubinin et al. 2018; L. Chai et al. 2019; N. Romanelli et al. 2020), and their properties may be associated with the magnetotail twisting (K. Liu et al. 2009; R. Jarvinen et al. 2013).

Clearly, the exact causes of the Martian magnetotail twist remain to be identified. The present study employs self-consistent global hybrid simulations of the Martian magnetosphere to investigate the causes of its magnetotail twist. Four sets of simulations with/without crustal fields and planetary pickup ions and under different IMF conditions, have been carried out. In the rest of the paper, Section 2 introduces the simulation model and the simulation setups; the results of magnetotail twist in the four sets of simulations are presented and compared in Section 3 to assess the roles of the IMF, crustal fields, and planetary pickup ions in producing the twist; conclusions are finally summarized in Section 4.

2. Simulation Model and Setups

The simulations in the present study are performed using the RHybrid simulation platform, as in R. Jarvinen et al. (2018, 2022). The code represents plasma by implementing a macroparticle description for ions and a massless, charge-neutralizing fluid description for electrons. More details about the simulation algorithm can be found in E. Kallio & P. Janhunen (2002). The simulations are three-dimensional and use the planet-centered Mars solar orbital (MSO) coordinate system with aberration of a few degrees (caused by the motion of Mars around the Sun) neglected. The X-axis is antialigned with the undisturbed, upstream SW velocity (in exact MSO coordinates the X-axis points toward the Sun from Mars), the Z-axis points to the Martian ecliptic north, and the Y-axis completes the right-handed Cartesian set. As listed in Table 1, four groups of simulations with/without crustal fields and planetary pickup ions and under different IMF conditions, have been carried out. They have the same simulation domain: $-12\,R_M < X < 4\,R_M$, $-6\,R_M < Y < 6\,R_M$, and $-6\,R_M < Z < 6\,R_M$, where R_M is the radius of Mars. Note that the simulation domain extends deep into the magnetotail in order to examine the tail twist. The simulation domain is partitioned into small cubic cells with a side length of $0.08\,R_M$, and the simulation time step is 20 ms. The upstream SW has a number density of $4\,\mathrm{cm}^{-3}$, a temperature of 1×10^5 K, and a bulk velocity of $380\,\mathrm{km\,s}^{-1}$ in the $-X$-direction. Following G. A. DiBraccio et al. (2018), the upstream IMF is set at a fixed magnitude of 3 nT and its vector is contained in the XY plane and varies between two conditions: (−1.6, 2.5, 0) nT and (1.6, −2.5, 0) nT. These two IMF conditions correspond to Parker spiral angles of 57° and −123°. They are referred to as $+B_Y$ IMF and $-B_Y$ IMF, respectively, in the rest of the paper.

Table 1
Setups of the Four Groups of Simulations

Simulation Group	Run	IMF Orientation	Crustal Magnetic Fields	Planetary Pickup Ions
A	A1	$+B_Y$	Nightside	Y
	A2	$+B_Y$	Dayside	…
	A3	$-B_Y$	Nightside	…
	A4	$-B_Y$	Dayside	…
B	B1	$+B_Y$	N	Y
	B2	$-B_Y$	…	…
C	C1	$+B_Y$	Nightside	N
	C2	$+B_Y$	Dayside	…
	C3	$-B_Y$	Nightside	…
	C4	$-B_Y$	Dayside	…
D	D1	$+B_Y$	N	N
	D2	$-B_Y$	…	…

Note. In this table, "$+B_Y$" and "$-B_Y$" represent $+B_Y$ IMF and $-B_Y$ IMF conditions as described in the text. "Dayside" and "Nightside" indicate that the region of strongest crustal field lies at noon and midnight, respectively. "N" in the fourth column denotes that the crustal magnetic fields are not included in the simulations. "Y" and "N" in the last column indicate that the planetary pickup ions are included and excluded in the simulations, respectively.

The first group (Group A) of simulations take into account the crustal magnetic fields and planetary pickup ions. The crustal fields in the present study come from the 110-order spherical harmonic model in J. W. Gao et al. (2021). Four simulations in the first group correspond to the four combinations of $+B_Y$ IMF/$-B_Y$ IMF and dayside/nightside crustal fields. Here the dayside/nightside crustal fields mean that the region of strongest crustal field is at noon and midnight, respectively. In addition, the simulations contain planetary pickup ions, including O^+, and O_2^+ from the ionosphere and H^+ and O^+ from the exosphere. The pickup ions of ionospheric origin are modeled as ions emitted from a spherical inner boundary at a distance of 400 km above Mars' surface. The emission has a cosine dependence on the solar zenith angle on the dayside and remains constant on the nightside. It peaks at noon and gradually decreases to just 10% of its noontime peak intensity at the terminator. The global production rates of ionospheric ions are set as $8 \times 10^{24}\,\mathrm{s}^{-1}$ for O^+ and $1 \times 10^{25}\,\mathrm{s}^{-1}$ for O_2^+. On the other hand, the pickup ions of exospheric origin are generated in the system by photoionization from the exospheric neutral profiles of "Run B (solar min, with exosphere)" of the "Intercomparison of Global Models and Measurements of the Martian Plasma Environment" International Space Science Institute team's second meeting (D. Brain et al. 2010; R. Jarvinen et al. 2022). The global production rates of exospheric ions are set as $1 \times 10^{24}\,\mathrm{s}^{-1}$ for H^+ and $2 \times 10^{24}\,\mathrm{s}^{-1}$ for O^+. For simplicity, the photoionization rate remains constant above the inner boundary, but no photoions are generated in the planetary shadow. In addition, there is a spherical, absorbing inner boundary 200 km above Mars' surface. Particles reaching this boundary are removed from the system. All simulation parameters are stationary in the runs analyzed here.

In order to isolate and compare the influences of the crustal fields and the planetary pickup ions, three extra groups of simulations (beyond Group A) are performed, as listed in Table 1. The simulations in the second group (Group B) do not consider the crustal fields. On the other hand, the planetary pickup ions are turned off in the simulations of the third group

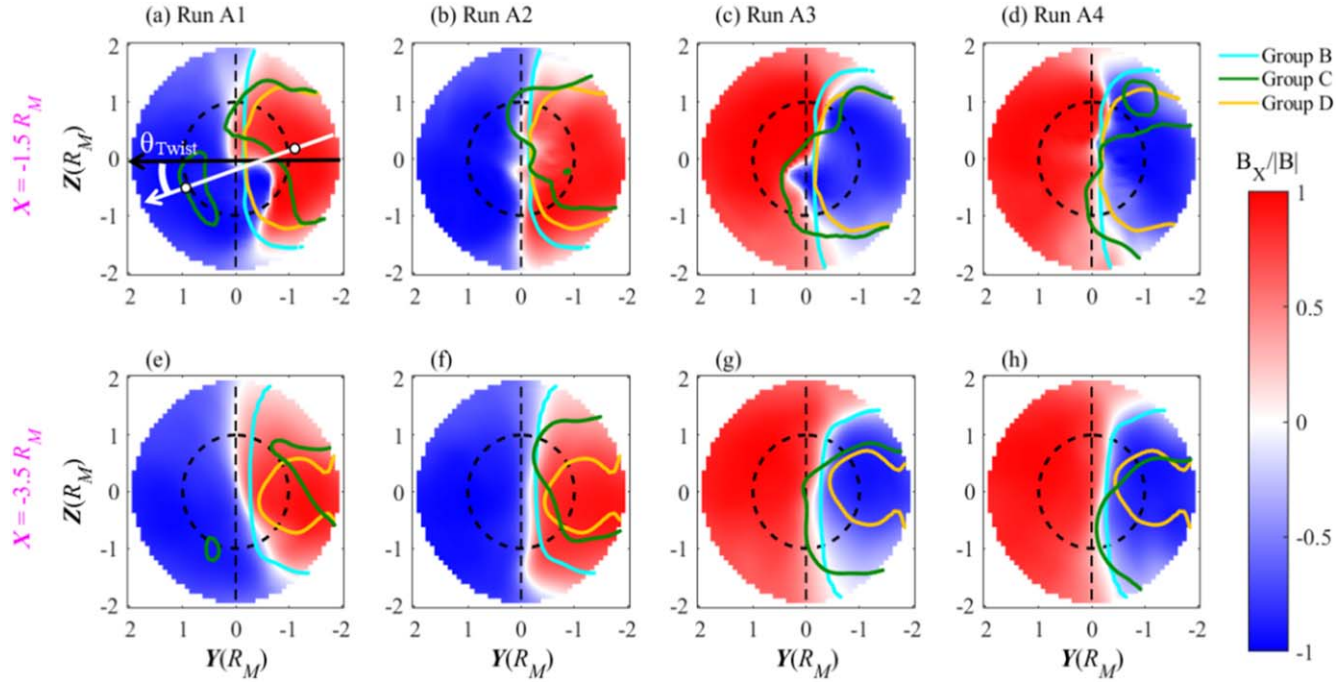

Figure 1. *YZ* cuts of the normalized B_X at $X = -1.5\ R_M$ ((a)–(d)) and $-3.5\ R_M$ ((e)–(h)) in the four simulations of Group A, as labeled on the top of each column. The overlaid cyan, green, and yellow curves in each panel represent the locations of the neutral current sheet in the corresponding simulations with the same conditions of the IMF and crustal fields (if included) in Groups B, C, and D, respectively. They are to be compared with the white region separating the positive lobe ($+B_X$, red area) and negative lobe ($-B_X$, blue area) in the same panel, which indicates the position of the neutral sheet in an individual simulation of Group A. In addition, the black dashed circle represents Mars' shadow and the vertical dashed line is at $Y = 0$. Finally, the white and black arrows in (a) depict how the twist angle ($\theta_{\rm Twist}$) is defined (see text for details).

(Group C). Finally, the simulations in the fourth group (Group D) have neither the crustal fields nor the planetary pickup ions. Note that Groups B and D each contain two simulations corresponding to $+B_Y$ IMF and $-B_Y$ IMF, while Group C has four simulations with IMF and crustal field conditions matching the four simulations in Group A.

3. Simulation Results

3.1. Magnetotail Twist in Different Simulations

As in G. A. DiBraccio et al. (2018), the Martian magnetotail twist is examined in the present study by showing the *YZ* cross sections of the normalized B_X, the *X*-component of the magnetic field normalized to the total magnetic field ($B_X/|B|$), in the magnetotail. The first and second rows of Figure 1 display the *YZ* cuts of the normalized B_X at $X = -1.5$ and $-3.5\ R_{\rm M}$ in the four simulations of Group A, respectively, with a spatial constraint $\sqrt{Y^2 + Z^2} \leqslant 2R_{\rm M}$ to focus on the region of interest. According to the color bar on the right, the red and blue regions in each panel correspond to the positive and negative lobes with $+B_X$ and $-B_X$, respectively, and the white area between them depicts the location of the neutral sheet. In addition, the black dashed circle represents the shadow of Mars and the vertical dashed line at $Y = 0$ indicates the traditionally expected, hemispherically symmetric location of the neutral sheet of an ideal induced magnetosphere if the IMF has only a B_Y component (R. Jarvinen et al. 2013; A. R. Azari et al. 2023). To better illustrate the overall magnetotail twist, Figure 2 further presents the three-dimensional surface of the neutral sheet in Run A1 as an example. As Figure 2 shows, the neutral sheet in Run A1 is deflected from the $Y = 0$ plane and twisted into an "S" shape in the near-magnetotail region. The "S"-shaped twist diminishes as the downtail distance increases and the neutral sheet gradually changes into a slightly curved smooth surface oblique to the $Y = 0$ plane.

The normalized B_X maps at $X = -1.5\ R_{\rm M}$ in the four simulations of Group A (Figures 1(a)–(d)) demonstrate general agreement with the observed results in G. A. DiBraccio et al. (2018, 2022). The Martian magnetotail twists counterclockwise and clockwise for $+B_Y$ and $-B_Y$ IMF conditions, respectively. Interestingly, the twist is much more pronounced when the crustal fields are on the nightside (Figures 1(a) and (c)), while it becomes minimal when the crustal fields are on the dayside (Figures 1(b) and (d)). Although these results concur with G. A. Dibraccio et al. (2018, 2022) that the crustal fields affect the twist, they do not align with their explanation that the dayside magnetic reconnection between the crustal fields and draped IMF has caused the twist. Furthermore, following G. A. DiBraccio et al. (2022), the twist angle ($\theta_{\rm Twist}$) is calculated to quantify the Martian magnetotail twist in the simulations. As depicted in Figure 1(a), the geometric centroids of the positive and negative lobes (the two white dots) determine the lobe vector (the white arrow), and the angle between the lobe vector and the black vector along the *Y*-direction (which represents the expected direction of the lobe vector based on solely IMF draping) is defined as $\theta_{\rm Twist}$. In Figures 1(a)–(d) for Runs A1 to A4, $\theta_{\rm Twist} = 23.^{\circ}3$, $8.^{\circ}4$, $14.^{\circ}1$, and $5.^{\circ}9$, respectively. In comparison, the statistical analysis of MAVEN observations in Figure 3(f) of G. A. Dibraccio et al. (2022) gives $\theta_{\rm Twist} \approx 27^{\circ}$ and 7° at $X = -1.5\ R_{\rm M}$ for $+B_Y$ IMF and $-B_Y$ IMF, respectively.

For comparison purposes, the locations of the neutral sheet in the corresponding simulations of the other three simulation groups are also plotted as the cyan, green, and yellow lines in

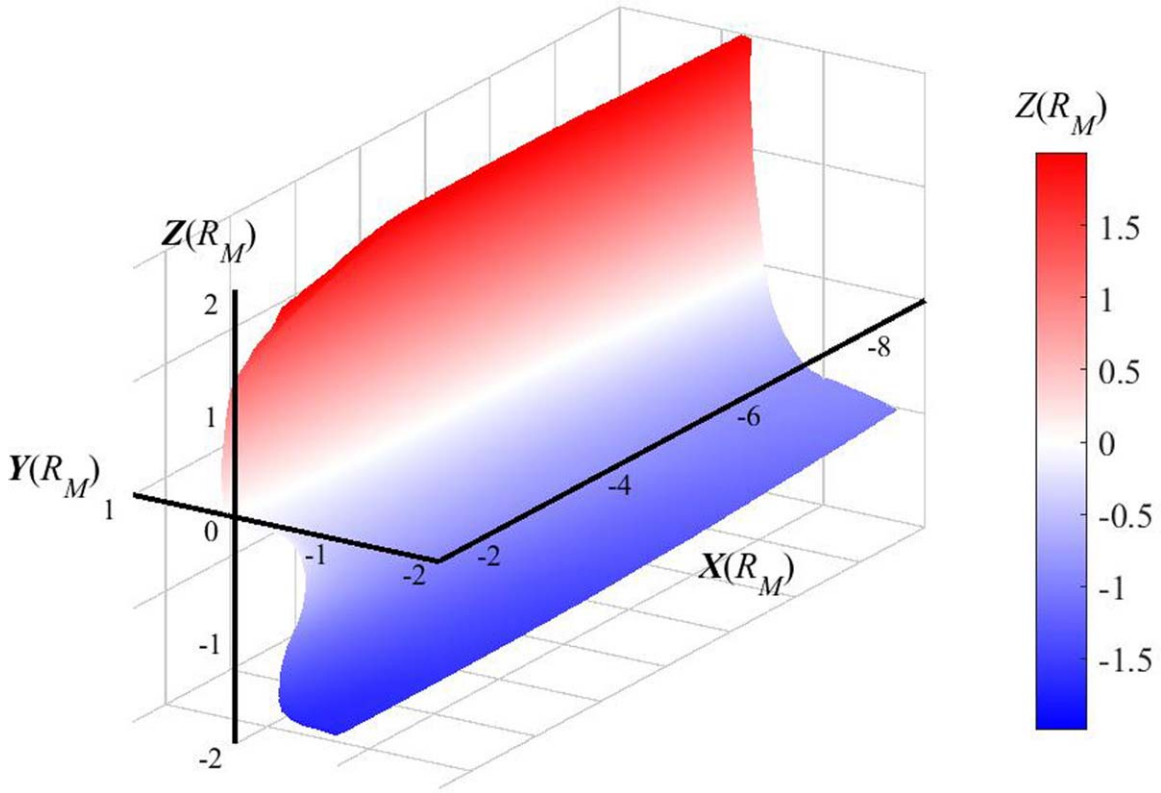

Figure 2. The three-dimensional surface of the neutral sheet in Run A1 to illustrate the overall magnetotail twist.

Figure 1, as indicated by the legend at the top right. In each panel, the simulations from the four groups have the same conditions of the IMF and crustal fields (if included), so the relative positions of the positive and negative lobes with respect to the neutral sheets remain unchanged (from what is shown for the run in Group A). Comparing the distorted neutral sheets at $X = -1.5\,R_M$ in the Group A simulations (the white areas in Figures 1(a)–(d)) with those in the simulations of other groups (the cyan, green, and yellow curves in Figures 1(a)–(d)) reveals that the Group A results better align with the green lines from Group C inside Mars' shadow. Outside the shadow, they follow the cyan lines from Group B more closely. As Table 1 shows, the simulations in Group B do not have the crustal fields and the ones in Group C do not include the planetary pickup ions. Thus, the above comparison indicates that in the near magnetotail at $X = -1.5\,R_M$, the magnetotail twist inside Mars' shadow is mainly attributable to the crustal fields, while the planetary pickup ions have a nonnegligible contribution outside the shadow.

Figures 1(e)–(h) display the normalized B_X maps further downstream of the magnetotail at $X = -3.5\,R_M$. The neutral sheets in the Group A simulations are less distorted than that at $X = -1.5\,R_M$. They match the cyan lines from Group B the best, whether inside or outside of Mars' shadow. This is especially true in Figures 1(f) and (h) when the crustal fields are on the dayside. Such a trend is consistent with the reduced contribution of the crustal fields to the magnetotail twist when they are on the dayside, as already demonstrated by Figures 1(a)–(d). In terms of the twist angle, θ_{Twist}= 20.°7, 6.°3, 14.°9, and 9.6° in Figures 1(e)–(h) for Runs A1 to A4, respectively. The θ_{Twist} values at $X = -3.5\,R_M$ are close to those at $X = -1.5\,R_M$. Indeed, θ_{Twist} does not significantly change with X in the simulations. This is in contrast to the trend shown in Figure 3(f) of G. A. Dibraccio et al. (2022) where the average θ_{Twist} calculated from MAVEN observations increases between $X = -1.6\,R_M$ and $X = -2.5\,R_M$ (for both $+B_Y$ IMF and $-B_Y$ IMF). The reason might be that the present simulations all have IMF $B_Z = 0$ for simplicity, but this parameter is mostly not zero in reality (see Figure 1(f) in G. A. Dibraccio et al. 2018) and has an important influence on θ_{Twist}. The influence of IMF B_Z on the Martian magnetotail twist will be further investigated in the future.

In addition, note that the two simulations in Group D have neither the crustal fields nor the planetary pickup ions. The results correspond to a purely induced magnetosphere and are approximately symmetric about $Z = 0$. The crescent-shaped neutral sheets shown by the yellow lines result from the draped IMF when it has a nonzero X-component, as explained in Figure 7 of A. R. Azari et al. (2023). It is also worth mentioning that the shapes of the neutral sheets in the two Group B simulations (B1 and B2) are roughly symmetric with each other about $Z = 0$ (e.g., see the cyan curves in Figures 1(a) and (c) or Figures 1(e) and (g). Runs B1 and B2 do not include the crustal fields and have $+B_Y$ IMF and $-B_Y$ IMF, respectively. Accordingly, the motional electric field in the SW is northward in Run B1 but flips to southward in Run B2. Under the influence of the motional electric field, the planetary pickup ions then escape from Mars mostly in the northern and southern hemispheres, respectively, in the two simulations. This correspondence makes the resultant neutral sheets nearly symmetric to each other about $Z = 0$.

3.2. Contribution of the Planetary Pickup Ions

It is clear from Figure 1 that, besides the IMF and the crustal fields, the planetary pickup ions also contribute to the distortion

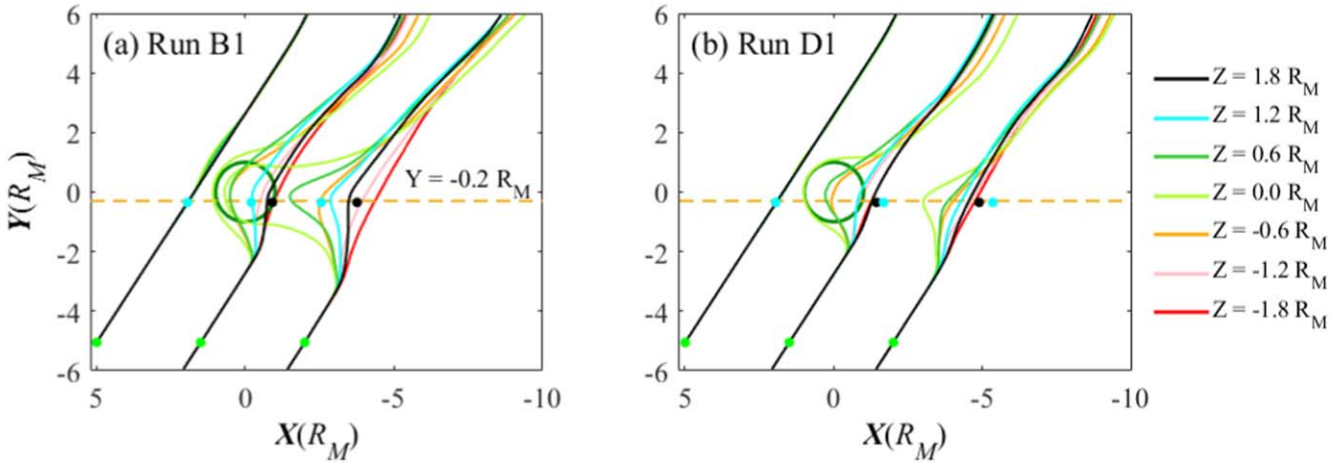

Figure 3. The projection of three sets of magnetic field lines in (a) Run B1 and (b) Run D1 onto the *XY* plane. The magnetic field lines in one specific set all go through a group of points with the same *X*- and *Y*-values but different *Z*-values (as indicated by the green points). Each set contains seven lines in different colors according to their *Z*-values, as labeled on the right. The orange dashed lines mark the location of $Y = -0.2\ R_M$. The black and cyan dots on the orange dashed lines illustrate the SW flow at $Z = 1.8$ and $1.2\ R_M$, respectively (see text for details). The black circle around the origin in each panel represents Mars.

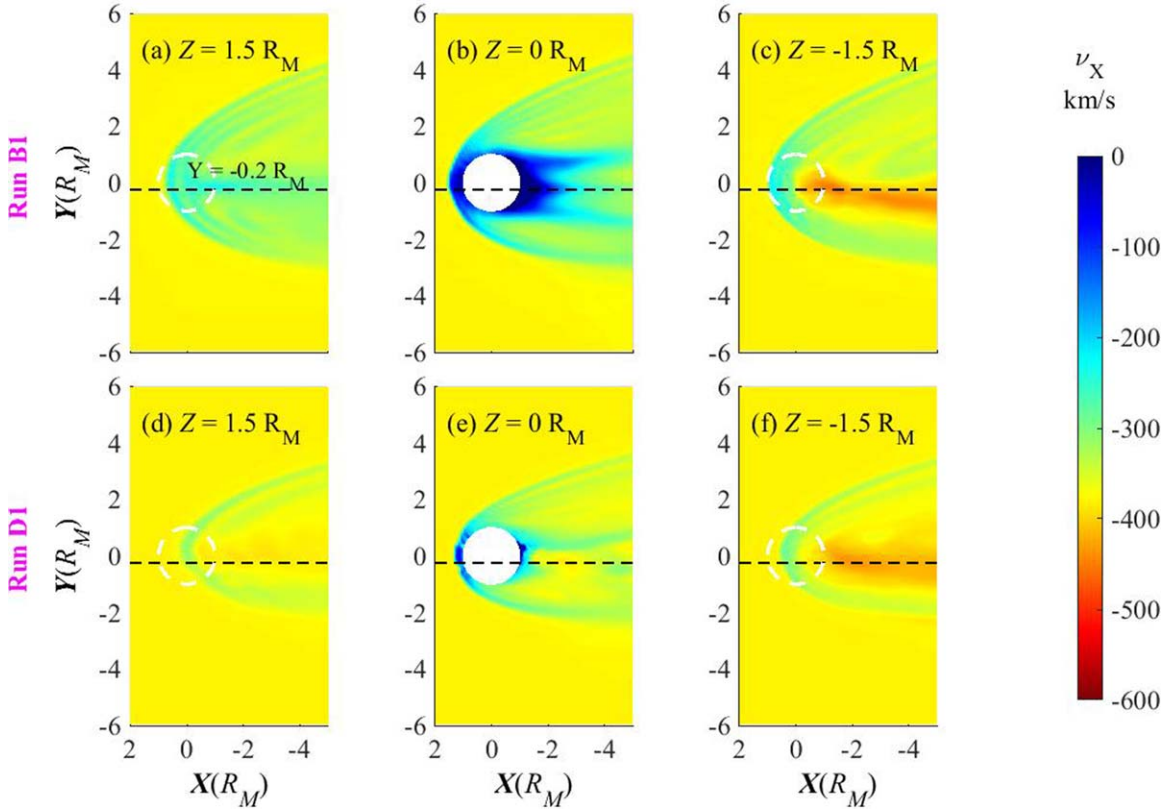

Figure 4. Maps of the *X*-component of the SW ion flow velocity ($V_{X,SW}$) in the *XY* plane at three different *Z*-values (as labeled) in Runs B1 (top) and D1 (bottom). In each panel, the horizontal black dashed line indicates $Y = Y_{NS}$, while the white circle represents the projection of Mars.

of the neutral sheet in the Martian magnetotail. The distortion inside Mars' shadow in the near magnetotail at $X = -1.5\ R_M$ is mainly attributable to the crustal fields, but the influence of the crustal fields diminishes at locations further away from Mars. The contribution of the pickup ions prevails in the far magnetotail at $X = -3.5\ R_M$. To investigate how the planetary pickup ions deform the neutral sheet in the Martian magnetotail, Figures 3(a) and (b) display three sets of magnetic field lines in Runs B1 and D1, respectively. The magnetic field lines in one specific set go through a group of points with the same *X*- and *Y*-values but different *Z*-values (as indicated by the green points). Each set contains seven lines in different colors according to their *Z*-values, as marked on the right. In both Runs B1 and D1, the presence of Mars slows down the downstream convection of the magnetic field lines, especially within Mars' shadow, and causes them to bend toward the Sun. On the other hand, the magnetic field lines in Run B1 exhibit a clear bending asymmetry between the $\pm Z$ hemispheres, with

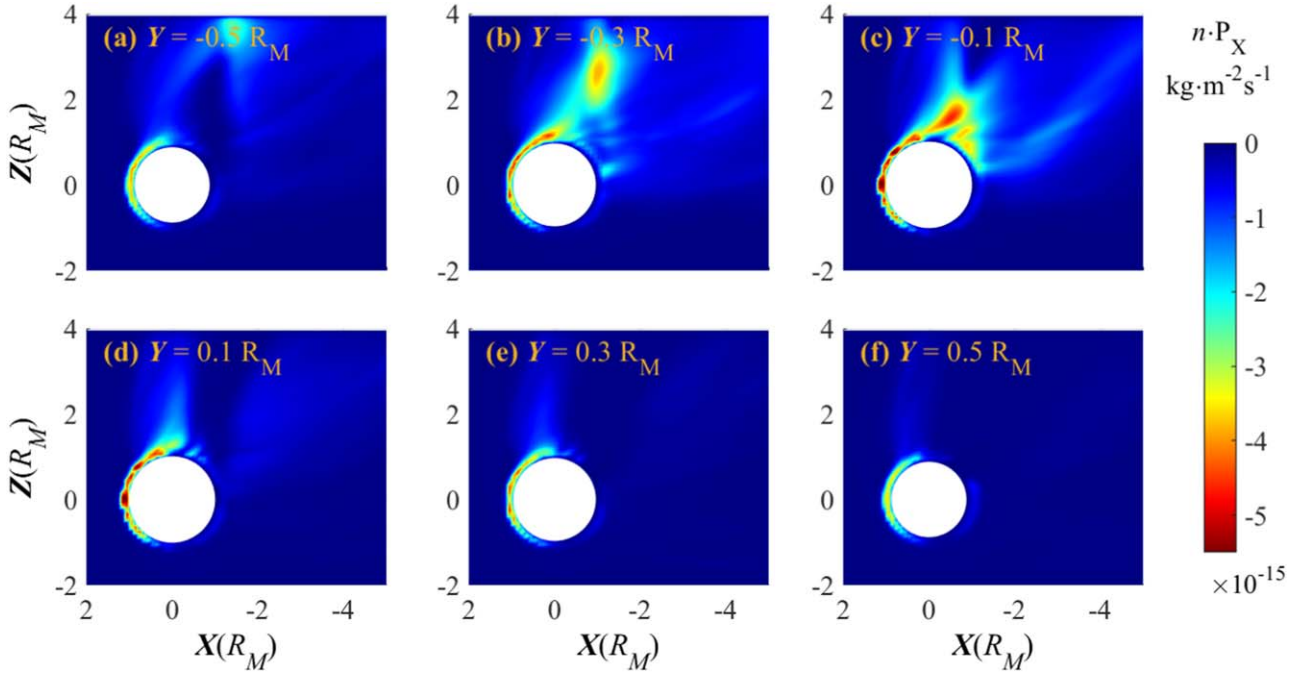

Figure 5. *XZ* cuts of the *X*-component of the planetary ion momentum density in Run B1 at different *Y*-values as labeled. The white circle represents Mars in each panel.

the draping of the magnetic field lines more pronounced in the $+Z$ hemisphere. Since the location of the neutral sheet is related to the turning point in a magnetic field line where B_X switches its sign, the enhanced bending of the magnetic field lines around $Y = 0$ in the $+Z$ hemisphere makes the neutral sheet shift toward $Y = 0$ in Run B1 (as shown by the cyan curves in Figures 1(a) and (e)), in comparison with that in Run D1 (the yellow curves in Figures 1(a) and (e)). This further produces a relative shift of the positive lobe in the $+Z$-direction and hence a twist of the Martian magnetotail, consistent with the results of observations in Figure 11 of Z. J. Rong et al. (2016) for the Venusian magnetotail. In addition, the negative B_X of the IMF leads to a shift of the neutral sheet in the $-Y$-direction from its expected location of $Y = 0$ when IMF $B_X = 0$, as already demonstrated in R. Jarvinen et al. (2013), M. Delva et al. (2017), and Y. Li et al. (2021). As marked by the orange dashed line in Figure 3(a) and shown by the cyan lines in Figures 1(a) and (e), the neutral sheet in the $+Z$ hemisphere lies around $Y = -0.2\,R_M$ in Run B1. This *Y*-value is referred to as Y_{NS} in the rest of the paper and also marked in Figure 3(b) as the orange dashed line for comparison purposes.

For large-scale and slowly varying plasma processes, ideal MHD approximately holds and magnetic field lines are "frozen in" the plasma flow. Thus, the bending of the magnetic field lines shown in Figures 3(a) and (b) is likely associated with the plasma flow in these simulations. Figure 4 presents the *X*-component of the SW ion flow velocity ($V_{X,SW}$) in the *XY* plane at three different *Z*-values (as labeled) in Runs B1 and D1. Note that the ions that originate from the upstream SW are always referred to as SW ions in the present study, even after they have entered the Martian magnetosphere. Consistent with the bending asymmetry of the magnetic field lines between the $\pm Z$ hemispheres in Run B1 (Figure 3(a)), $V_{X,SW}$ is significantly different at $Z = 1.5\,R_M$ (Figure 4(a)) and $Z = -1.5\,R_M$ (Figure 4(c)). The magnitude of $V_{X,SW}$ near $Y = Y_{NS}$ (indicated by the horizontal black dashed line) in the tail in Figure 4(a) is notably smaller than that in Figure 4(c). In addition, Figure 4(a) shows that the magnitude of $V_{X,SW}$ around $Y = Y_{NS}$ in the tail is smaller than in the regions above and below. Interestingly, the opposite is true for $V_{X,SW}$ shown in Figure 4(c) for $Z = -1.5\,R_M$. In contrast, the difference between $V_{X,SW}$ at $Z = 1.5\,R_M$ (Figure 4(d)) and $Z = -1.5\,R_M$ (Figure 4(e)) in Run D1 is less pronounced. There is no slowing down of the SW near $Y = Y_{NS}$ in the tail at $Z = 1.5\,R_M$ (Figure 4(d)). This is in line with the magnetic field lines being approximately symmetric between the $\pm Z$ hemispheres in Run D1, as shown in Figure 3(b).

With the $V_{X,SW}$ results available, the SW ion flow can be tracked in the simulations to check whether magnetic field lines are frozen in the SW plasma flow. In both panels of Figure 3, the black and cyan dots on the orange dashed line illustrate the SW flow along $Y = Y_{NS}$ at $Z = 1.8$ and $1.2\,R_M$, respectively, at three different times. In the beginning, the black and cyan dots are on the two magnetic field lines with the corresponding colors in the leftmost set. Note that this set of magnetic field lines are not yet disturbed much by Mars. They overlay each other in the *XY* plane despite their different *Z*-values. Subsequently, the black dot is indeed covered by the cyan dot initially. Later, when the SW parcel represented by the leftmost green point moves to its new locations represented by the two green dots at smaller *X*-values on the right, the new locations of the SW plasma parcels corresponding to the leftmost cyan (and black) dots are marked by the subsequent dots of the same colors on the right as well. The fact that the black and cyan dots remain close to the magnetic field lines of the same colors at the two later times suggests that the magnetic field lines are roughly frozen in the SW flow in the simulations. Thus, the enhanced bending of the magnetic field lines in the $+Z$ hemisphere in Run B1 mostly comes from the SW slowing down in the region.

The difference between the setups of Runs B1 and D1 is the planetary pickup ions. Previous studies have suggested that the

momentum exchange between the pickup ions and the SW can cause the SW to slow down and deflect (N. Romanelli et al. 2020; Y. Liu et al. 2024). Therefore, the slowing down of the SW near $Y = Y_{NS}$ in the tail at $Z = 1.5\ R_M$ in Run B1 is likely due to the mass loading of the planetary pickup ions. This is indeed confirmed by Figure 5, which shows the XZ cuts of the X-component of the momentum density of the planetary pickup ions in Run B1 at different Y-values as labeled. Consistent with previous studies (e.g., R. Jarvinen et al. 2018), the escape (and mass loading) of the planetary pickup ions mainly occurs near $Y = Y_{NS}$ in the hemisphere where the SW motional electric field points away from the planet (the $+Z$ hemisphere in Run B1). Thus, the planetary pickup ions can modify the topology of the magnetic field lines in the Martian magnetotail by affecting the SW flow velocity. This, in turn, contributes to the Martian magnetotail twist, besides the IMF and the crustal fields.

4. Conclusions

Three-dimensional global hybrid simulations have been carried out using the RHybrid simulation platform to investigate the causes of the Martian magnetotail twist. The comparison of the results from four groups of simulations with/without crustal fields and planetary pickup ions and under different IMF conditions, demonstrates that the IMF, crustal fields, and planetary pickup ions all affect the magnetotail twist. In agreement with previous studies, the crustal fields cause the Martian magnetotail to twist counterclockwise and clockwise for $+B_Y$ and $-B_Y$ IMF conditions, respectively. However, the twist is more pronounced when the crustal fields are on the nightside, in contrast with the early explanation that the crustal fields affect the twist through dayside magnetic reconnection between the crustal fields and the draped IMF. In addition, since the planetary pickup ions escape from Mars mainly in the hemisphere where the SW motional electric field points away from the planet, the mass loading of the pickup ions slows down the plasma flow in that region and causes the magnetic field lines "frozen in" the plasma flow to drag behind. This causes the Martian magnetotail to twist as well, even if there are no crustal fields. The simulation results further show that the distortion of the neutral sheet inside Mars' shadow in the near magnetotail at $X = -1.5\ R_M$ is mainly attributable to the crustal fields, but the influence of the planetary pickup ions starts to dominate outside Mars' shadow and at locations further away from Mars ($X = -3.5\ R_M$). Finally, in a purely induced magnetosphere (excluding the influences of the crustal magnetic fields and planetary pickup ions), the magnetotail remains largely symmetric about $Z = 0$. However, the presence of a nonzero IMF B_X shifts the neutral sheet in the $-Y$-direction and distorts it into a crescent shape, in comparison with the expected location of the neutral sheet at $Y = 0$ when IMF $B_X = 0$.

Acknowledgments

We wish to thank the Finnish Meteorological Institute for providing the RHybrid simulation platform, which is distributed under the open source GPL v3 license (github.com/fmihpc/rhybrid). The simulation code version used in this study (J. Zhou & R. Jarvinen 2024) is archived at doi:10.5281/zenodo.13706293. This work was supported by Strategic Priority Research Program of Chinese Academy of Sciences (grant No. XDB 41000000), the National Natural Science Foundation of China (NSFC) grant 42174203, the Guangdong Pearl River Talent Program (2019QN01G838), and Shenzhen Science and Technology Program (grant JCY20210324104810027). R.J. received funding from the European Research Council (grant agreement No. 101124960). It was also supported by the Center for Computational Science and Engineering of Southern University of Science and Technology.

ORCID iDs

Jingyi Zhou https://orcid.org/0009-0000-9868-5666
Kaijun Liu https://orcid.org/0000-0001-5882-1328
Riku Jarvinen https://orcid.org/0000-0002-4246-2954
Kun Cheng https://orcid.org/0000-0003-1019-2598
Shuai Zhang https://orcid.org/0000-0001-8006-1177
Qi Liu https://orcid.org/0000-0003-0474-0260
Yuqi Liu https://orcid.org/0000-0002-7120-003X
Yan Wang https://orcid.org/0000-0001-6783-7591

References

Acuña, M. H., Connerney, J. E.-P., Ness, N. F., et al. 1999, Sci, 284, 790
Azari, A. R., Abrahams, E., Sapienza, F., et al. 2023, JGRA, 128, e2023JA031546
Brain, D., Barabash, S., Boesswetter, A., et al. 2010, Icar, 206, 139
Brecht, S. H. 1990, GeoRL, 17, 1243
Chai, L., Wan, W., Wei, Y., et al. 2019, ApJL, 871, L127
Delva, M., Volwerk, M., Jarvinen, R., et al. 2017, JGR, 122, 10
DiBraccio, G. A., Luhmann, J. G., Curry, S. M., et al. 2018, GeoRL, 45, 4559
DiBraccio, G. A., Romanelli, N., Bowers, C. F., et al. 2022, GeoRL, 49, e2022GL098007
Dong, C., Bougher, S. W., Ma, Y., et al. 2015, JGR, 120, 7857
Dubinin, E., Fraenz, M., Pätzold, M., et al. 2018, GeoRL, 45, 2574
Dubinin, E., Fraenz, M., Pätzold, M., et al. 2022, JGRA, 128, e2022JA030575
Gao, J. W., Rong, Z. J., Klinger, L., et al. 2021, E&SS, 8, e2021EA001860
Garnier, P., Jacquey, C., Gendre, X., et al. 2022, JGRA, 127, e2021JA030146
Hara, T., Harada, Y., Mitchell, D. L., et al. 2017, GeoRL, 44, 7653
Harada, Y., Halekas, J. S., McFadden, J. P., et al. 2015, GeoRL, 42, 8838
Jarvinen, R., Brain, D. A., Modolo, R., et al. 2018, JGR, 123, 1678
Jarvinen, R., Kallio, E., & Dyadechkin, S. 2013, JGR, 118, 4551
Jarvinen, R., Kallio, E., & Pulkkinen, T. I. 2022, JGRA, 127, e2021JA030078
Kallio, E., Barabash, S., Janhunen, P., et al. 2008, P&SS, 56, 823
Kallio, E., & Janhunen, P. 2002, JGR, 107, 1035
Li, Y., Lu, H., Cao, J., et al. 2021, ApJ, 921, 139
Lillis, R. J., Frey, H. V., & Manga, M. 2008, GeoRL, 35, L14203
Liu, K., Kallio, E., Jarvinen, R., et al. 2009, AdSpR, 43, 1436
Liu, Y., Liu, K., Lu, D., et al. 2024, ApJ, 962, 127
Pitkänen, T., Kullen, A., Cai, L., et al. 2021, GSL, 8, 3
Ramstad, R., Brain, D. A., Dong, Y., et al. 2020, NatAs, 4, 979
Romanelli, N., Bertucci, C., Gómez, D., et al. 2015, JGR, 120, 7737
Romanelli, N., DiBraccio, G., Halekas, J., et al. 2020, GeoRL, 47, e2020GL090793
Romanelli, N., DiBraccio, G. A., Slavin, J., et al. 2022, GeoRL, 49, e2022GL101643
Rong, Z. J., Stenberg, G., Wei, Y., et al. 2016, JGR, 121, 10
Wang, M., Xu, X., Lee, L. C., et al. 2022, A&A, 667, A41
Xiao, S. D., Zhang, T. L., & Baumjohann, W. 2016, JGR, 121, 4542
Xu, S., Mitchell, D. L., Weber, T., et al. 2020, JGRA, 125, e2019JA027755
Zhang, C., Rong, Z., Klinger, L., et al. 2022, JGRE, 127, e2022JE007334
Zhou, J., & Jarvinen, R. 2024, Rhybrid Code and Parameter Table v1, Zenodo, doi:10.5281/zenodo.13706293